# Real-time visualization of perforin nanopore assembly

Carl Leung[1,2,‡], Adrian W. Hodel[1,3,‡], Amelia J. Brennan[4,‡], Natalya Lukoyanova[2,‡], Sharon Tran[4], Colin M. House[5], Stephanie C. Kondos[6], James C. Whisstock[6,7], Michelle A. Dunstone[6,7,8], Joseph A. Trapani[5,9], Ilia Voskoboinik[4,9,]*, Helen R. Saibil[2,]* & Bart W. Hoogenboom[1,3,10,]*

[1]London Centre for Nanotechnology, University College London, London, United Kingdom
[2]Department of Crystallography/Biological Sciences, Institute of Structural and Molecular Biology, Birkbeck College, London, United Kingdom
[3]Institute of Structural and Molecular Biology, University College London, London, United Kingdom
[4]Killer Cell Biology Laboratory, Peter MacCallum Cancer Centre, East Melbourne, Australia
[5]Cancer Cell Death Laboratory, Peter MacCallum Cancer Centre, East Melbourne, Australia
[6]Department of Biochemistry and Molecular Biology, Monash University, Clayton, Melbourne, Australia
[7]The ARC Centre of Excellence in Advanced Molecular Imaging, Monash University, Melbourne, Australia
[8]Department of Microbiology, Monash University, Melbourne, Australia
[9]Sir Peter MacCallum Department of Oncology, University of Melbourne, Melbourne, Australia
[10]Department of Physics and Astronomy, University College London, London, United Kingdom

[‡]These authors contributed equally to this work.
*Corresponding authors: ilia.voskoboinik@petermac.org (I.V.); h.saibil@mail.cryst.bbk.ac.uk (H.R.S.); b.hoogenboom@ucl.ac.uk (B.W.H.).

**Perforin is a key protein of the vertebrate immune system. Secreted by cytotoxic lymphocytes as soluble monomers, perforin can self-assemble into oligomeric pores of 10-20 nm inner diameter in the membranes of virus-infected and cancerous cells. These large pores facilitate the entry of pro-apoptopic granzymes, thereby rapidly killing the target cell. To elucidate the pathways of perforin pore assembly, we have carried out real-time atomic force microscopy and electron microscopy studies. Our experiments reveal that the pore assembly proceeds via a membrane-bound prepore intermediate state, typically consisting of up to ~8 loosely but irreversibly assembled monomeric subunits. These short oligomers convert to more closely packed membrane nanopore assemblies, which can subsequently recruit additional prepore oligomers to grow the pore size.**

Perforin is a pore-forming protein that is expressed in cytotoxic lymphocytes and that is secreted, together with the pro-apoptotic serine proteases granzymes, into the immune synapse formed between the lymphocyte and a cognate virus-infected or cancerous cell. The loss of perforin expression or function is catastrophic and leads to fatal immune dysregulation[1]. Perforin is part of the Membrane Attack Complex/Perforin/Cholesterol-Dependent Cytolysin (MACPF/CDC) superfamily[2,3]. This superfamily also includes the terminal components of the complement pathway in the immune system, as well as the CDC family of bacterial toxins. The pore-forming mechanism of the superfamily involves the unravelling of two α-helical regions that refold into transmembrane hairpins (TMH1 and TMH2). These create giant β-barrel transmembrane pores up to 30 nm in diameter, formed of up to 50 monomers (in the case of CDCs).

The pathways of CDC assembly have been extensively characterized. CDCs first form differently sized assemblies in a prepore intermediate state on the membrane. The prepore oligomers subsequently undergo a cooperative vertical collapse and insertion of subunits into the membrane, resulting in arc- and ring-shaped pores[4-14].

By contrast, the pathways of MACPF assembly remain largely unclear, despite recent advances in the structural characterization of perforin[15] and MAC[16,17] pores. Structurally, MACPF proteins differ from CDCs in forming membrane-spanning β-barrels without vertical subunit collapse: Unlike CDCs, (the structurally characterized) MACPFs have transmembrane hairpins that are sufficiently long to span the membrane without such a collapse. The two-component fungal MACPF protein pleurotolysin can form fully assembled prepore intermediates on the target membrane, in common with the CDCs[18], but such prepore intermediates have yet to be observed for MAC and perforin. Moreover, binding assays[19] and structural data[16,17,20] on MAC components indicate that – unlike the CDCs[10] – the MAC can continue to assemble after insertion into the membrane. This argues for a growing-pore instead of the CDC growing-prepore mechanism; similar suggestions have been made for perforin[21,22].

Such mechanistic differences may have important physiological implications. A growing-pore mechanism would explain how membrane insertion of the C5b-C8 initiation complex triggers the recruitment of multiple copies of C9 protein to complete the hetero-oligomeric MAC pore[16,17,19,20], thus facilitating antimicrobial attack. For perforin, the assembly mechanism must be sufficiently rapid to allow efficient diffusion of granzymes into the target cell within the time frame (< 20 sec) of the membrane-repair response of virus-infected and cancerous target cells to perforin pore formation[23]. In view of the limited understanding of perforin pore assembly and the key role of perforin in the immune system[1], this study is aimed at elucidating the pathways of perforin self-assembly into membrane-spanning oligomeric pores.

## Perforin assemblies on and in the target membrane

Atomic force microscopy (AFM) provides direct visualization of pore assembly, as has been demonstrated for CDCs by real-time imaging of membrane pore formation at nanometre resolution[7,10,12-14,24]. When imaged by AFM on a supported lipid bilayer, wild-type (WT) perforin forms a heterogeneous distribution of arc- and ring-shaped assemblies with a variable radius of curvature and a height of 11 nm[15,21] (Fig. 1a). This heterogeneous distribution is at least qualitatively consistent between experiments on supported lipid membranes, on liposomes, and on live cells[15,21,22], and the observed height is approximately equal to the height of a perforin monomer. When imaged with high aspect-ratio AFM probes, both arc and ring assemblies are found to locally remove and thus fully perforate the membrane in the pore lumen (Fig. 1b-e). Membrane perforation by arc assemblies is in line with earlier observations based on electrophysiology measurements on perforin[21] and based on direct AFM visualization of pore lumens for CDCs[10,12,13]. The formation of arc-shaped pores thus appears to be a widespread feature in MACPF/CDC pore formation[25].

To distinguish between different stages of membrane pore formation, a disulphide bond was engineered in perforin to inhibit membrane insertion without affecting the monomer-monomer interaction. Mass spectrometry was used to verify the presence of the additional disulphide bond in the mutant (Supplementary Fig. 1), beyond the 8 disulphide bonds already present in WT perforin. This engineered disulphide bond tethers the TMH1 region such that it is unable to reach the membrane (Fig. 2a), similar to previous constructs for CDCs[6,10] and pleurotolysin[18]. Without the reducing agent dithiothreitol (DTT), the TMH1-lock (A144C-W373C) mutant binds to the membrane in the presence of $Ca^{2+}$, but remains completely inactive (standardized haemolysis[26] < 4%; 100% refers to WT activity in control experiments). Pre-incubation of perforin with DTT led to a decrease in WT activity with increasing DTT concentration, suggesting that – under those conditions, which were avoided hereafter – the stability of the protein was affected by the reduction of the native disulphide bonds. Once TMH1-lock protein was bound to the membrane, however, its activity on post-incubation with DTT was identical to that of WT protein without DTT, for a wide range of protein and DTT concentrations (Supplementary Fig. 2).

Membrane-bound TMH1-lock perforin is detectable in AFM images by the presence of diffuse features or plateaus above the level of the membrane surface (Fig. 2b). These diffuse, mobile features can be induced to convert into static pores (similar to WT pores, Fig. 1) by the addition of DTT (Supplementary Movie 1). To more easily characterize the diffuse (and presumably not membrane-inserted) state by AFM, we restricted its diffusion to membrane domains in phase-separated lipid membranes[27], making use of the preference of perforin to bind to more loosely packed (here: PC-rich, lower domains in Fig. 1) lipid phases[28]. This caused the membrane bound TMH1-lock perforin to appear as featureless plateaus with a height of 11 nm above the membrane (Supplementary Fig. 3), consistent with the height of the perforin monomer[15].

Based on these results, we distinguish between mobile proteins that are weakly bound to the membrane surface, and immobile, membrane-inserted pores. In this context, it is worthwhile to note that the membranes used here are too fluid to immobilize surface-bound, non-inserted perforin assemblies, as verified by fluorescence recovery after photobleaching of labelled lipids (Supplementary Fig. 4). This also suggests that immobilization of the membrane-inserted pore assemblies is due to their direct contact, across the membrane, with the mica substrate that supports the lipid bilayer in the AFM experiments. These observations are consistent with previous AFM experiments on CDC prepores, which showed high mobility at minute time scale, except when tightly packed on the membrane[7,10].

## Characterization of perforin prepores

We next set out to determine the oligomeric assembly state of the TMH1-lock perforin on the membrane. To image it at higher spatial resolution, we immobilized the membrane-bound TMH1-lock perforin by glutaraldehyde fixation. In the resulting AFM images (Fig. 2c and Supplementary Fig. 5-6), the protein is found to have formed linear and curved prepore assemblies that are markedly shorter and less regularly shaped than WT perforin pores (Fig. 1). This observation was confirmed by negative stain electron microscopy (Fig. 2d). In all these experiments, unfixed membrane-bound prepores could be converted to static pores by exposure to DTT (Fig. 2e-h).

For a more quantitative analysis of subunit packing and assembly size, we calculated single-particle averages of short segments of perforin prepore and pore arcs and rings, and measured lengths of perforin assemblies from the electron microscopy images. Initially (≤15 min, 37 $^{o}$C; as in Fig. 2b-d), TMH1-lock perforin assembles as short, membrane-bound prepore oligomers with loose subunit packing (centre-to-centre spacing ± standard deviation: 3.86 ± 0.13 nm; Fig. 3a). With longer incubation times (50 min, 37 $^{o}$C), it evolves into a larger and more densely packed late prepore intermediate (2.89 ± 0.22 nm; Fig. 3b). Upon exposure to DTT, it shows the tight packing (2.55 ± 0.08 nm; Fig. 3c) seen in WT perforin pores (2.55 ± 0.09 nm; Fig. 3d). On average, the denser packing coincides with increasing assembly size (Fig. 3e-h) and formation of the pore β-barrel (Fig. 3c, d). After exposure to DTT, the TMH1-lock mutant shows a similar distribution of assembly sizes as the WT protein (Fig. 3g, h), except for the relatively high amount of short (2~6 subunits) assemblies, suggesting slow or incomplete reduction of the disulphide lock. Additional class averages for each condition can be found in Supplementary Fig. 7.

The discovery of loosely packed intermediates raises the question of whether their assembly is reversible. We first noted that the shape of the prepore assembly distributions (Fig. 3e, f) is consistent with the predictions for assembly growth by irreversible monomer association[10]. Next, focussing on conditions under which the early, most loosely packed prepore state prevails (15 min incubation at 37 °C; Figs. 2b-d, 3a, e), we hypothesized that irreversible prepore assembly would impair WT pore formation on co-incubation (and thus on co-assembly) with the TMH1-lock mutant. Such an effect has been previously demonstrated for the CDC suilysin[10]. On the other hand, a reversible assembly process would allow a free exchange of WT and TMH1-lock proteins in an assembly (as, e.g., shown for mutants of the CDC perfringolysin O [29]), leading to the formation of assemblies with sufficient WT content to irreversibly transit into transmembrane pores.

Experimentally, we found that in non-reducing conditions the addition of TMH1-lock protein indeed prevents co-assembled WT perforin from membrane insertion, in a dose-dependent manner (Fig. 4a, -DTT). Perforin pore formation was restored upon subsequent unlocking of the mutant with DTT: This excludes nonspecific aggregation as a cause of the inhibitory effect of TMH1-lock on the WT protein (Fig. 4a, +DTT). In additional control experiments, the WT perforin and the unlocked TMH1 mutant (+DTT) were found to have similar activity when incubated separately (Supplementary Fig. 2). These results were corroborated by *in-vitro* cell-based experiments, in which added TMH1-lock perforin inhibited the cytolytic activity of (a constant amount of) WT perforin in red blood cell lysis assays (Fig. 4b). In addition, in the context of the physiological immune synapse, cytotoxic activity was significantly lower for primary cytotoxic T lymphocytes that co-expressed both perforin variants, compared to cells expressing only WT perforin (Fig. 4c).

In the AFM images, we also observe the appearance of discrete assemblies with poorly resolved features that correlate with the fraction of TMH1-lock protein present (Fig. 4a, dotted circles). The localized nature of these assemblies indicates that they contain membrane-inserted subunits or are at least strongly interacting with such membrane-inserted pore subunits. However, their poorly resolved appearance implies that they retain some of the prepore mobility. We tentatively interpret these features as small pore assemblies that have nucleated further growth by association of TMH1-lock prepores to the transmembrane pore assembly.

## Real-time imaging of perforin pore assembly

Perforin pore assemblies could thus have a nucleating effect on the recruitment of the early prepores to the growing pore. To validate this interpretation, we visualized pore assembly of WT perforin in real time. For this purpose, we slowed the process by reducing the incubation temperature from 37 °C to 27 °C. This had the effect of slowing pore formation to tens of minutes, i.e., readily accessible within the time resolution of AFM experiments. At 27 °C, the early stages of incubation showed WT perforin appearing as diffuse plateaus on the membrane (Supplementary Figs. 8-9), which on fixation with glutaraldehyde appeared to largely consist of less regular, often shorter features of variable radius of curvature (Supplementary Fig. 8). This behaviour is fully consistent with our observations for the TMH1-lock perforin prepores, both for 27 °C and 37 °C incubations. With time, WT perforin transited from the diffuse, membrane-bound prepore state to immobile, hence membrane-inserted pore assemblies (Supplementary Fig. 9 and Supplementary Movie 2), resulting in a similarly heterogeneous distribution (see also Fig. 1a) of arc- and ring-shaped pores as observed for WT and TMH1-lock perforin after incubation at 37 °C.

The prepore intermediates and membrane-inserted pore assemblies at 27 °C thus appear fully consistent with the results for 37 °C incubations, but – because of the slowed kinetics – allowed us to track the assembly of individual pores in real time (Fig. 5, Supplementary Fig. 10, and Supplementary Movies 3-6). As before, we identify the static and sharply resolved assemblies as membrane-inserted pores, and observe how these pore assemblies grow by binding and immobilizing further oligomers from the surrounding, diffuse and mobile prepore state.

## Assembly pathways and physiological implications

Taken together, these results map out the hitherto unknown pathway of membrane pore assembly by the immune effector perforin. It has been previously shown that membrane binding of perforin monomers alone is not sufficient to trigger the conformational changes required for pore formation[30]. Perforin assembly is therefore critical for pore formation and for the attack of virus-infected and cancerous cells by the immune system[1]. However, we find that the completion of the assembly into ring-shaped pores is not a prerequisite: Fully consistent with previous observations for pore forming proteins, arc-shaped pores appear similarly effective in membrane perforation, creating pores with an unsealed lipid edge[10,12-14,21,22,24,25,31] (Fig. 1). For WT perforin, such incomplete, arc-shaped assemblies have previously been detected on liposomes and on nucleated cells[21,22]. While at the outset it was unclear how these structures would play a physiologically relevant role, further experiments indicated that the arc assemblies influence membrane remodelling and plasma membrane endocytosis, which can all facilitate granzyme uptake and apoptosis[21,22].

Our observations on the TMH1-lock mutant indicate that perforin initially forms early prepore assemblies on the membrane surface (Fig. 2a-d, Fig. 3a, e, and Supplementary Figs. 3, 5-7). These assemblies contain on average ~5 times fewer subunits and have a wider subunit spacing than pore assemblies (Fig. 3). This defines a new, early assembly intermediate, which is further confirmed by AFM images of WT perforin at reduced temperature (Supplementary Fig. 8). From the shape of the oligomeric distribution (Fig. 3e) and our results for co-assembly of WT and TMH1-lock protein (Fig. 4), we infer that this early prepore assembly is irreversible. This suggests that the perforin prepore assembly coincides with a conformational change that locks the subunits together, consistent with previous observations for the fungal MACPF protein pleurotolysin[18].

In some cases, the assembly process may proceed further without membrane insertion, to late prepore intermediates that more closely approach the size and subunit packing of pore assemblies, but lack the β-barrel (Fig. 3b, f). In general, however, we find marked differences in assembly size before and after membrane insertion (Fig. 2a-d vs Fig. 2g-h; Fig. 3a, e vs Fig. 3c, g). Specifically, we find that short, prepore assemblies convert to the pore state, and subsequently act as nucleation sites for the recruitment of additional prepore assemblies to the growing pore (Figs. 4, 5 and Supplementary Fig. 10). This prepore recruitment could occur via the membrane lesion and unsealed lipid edge that are caused by a growing pore assembly, and that trap additional prepores. This implies a cooperative, but sequential mechanism of membrane pore formation, where the pore assembly is greatly promoted upon membrane insertion of the short prepore arcs, and accompanied by significant changes in subunit packing.

These findings on MACPF protein perforin can be compared to previous findings on pore forming proteins of the MACPF/CDC superfamily, in particular to the bacterial CDCs, which have been extensively characterized. The early perforin prepore assemblies (Fig. 2a-d; Fig. 3a, e) may be compared to long, loosely bound assemblies of mutated perfringolysin O [29], but perforin differs by forming much shorter prepore assemblies that appear irreversibly bound. The larger and more tightly packed perforin late-prepore structures (Fig. 3b, f) resemble the prepore assemblies of the bacterial CDCs[4-10] and of MACPF pleurotolysin[18].

In our experiments, the membrane-insertion (and thus conversion to the pore state) of short perforin arc assemblies leads to the recruitment and association of other short prepore arc assemblies to the thus growing pore. This growing-pore mechanism is clearly distinct from CDCs, which oligomerize in the prepore state on the membrane (see also Supplementary Fig. 4). For the CDC suilysin, it was demonstrated that no further assembly occurs at all after membrane insertion[10]. For the CDC listerolysin O, more diverse behaviour has been observed by electrophysiology[32] and AFM[12-14] experiments. Listeriolysin O may tolerate subunit addition after pore formation, and shows a higher degree of interlocking of (mostly) large arc segments, leading to the suggestion of a hybrid growing-pore/growing-prepore mechanism[13]. However, recent high-speed AFM only showed oligomerization events in the prepore state, leading to the conclusion that the oligomerization and membrane insertion of listeriolysin O are spatiotemporally uncoupled[14]. This is similar to suilysin assembly and clearly different from perforin, for which we find a significant enhancement of assembly growth upon membrane insertion (see Fig. 2a-d vs Fig. 2g-h; Fig. 3a, e vs Fig. 3c, g; Figs. 4, 5 and Supplementary Fig. 10). This difference between perforin and CDC assembly may be attributed to the structural changes during membrane insertion. In particular, unlike MACPFs so far characterized, CDC assemblies can only form a membrane-spanning pore by collapsing towards the membrane surface, involving large subunit rearrangements. Interestingly, the differences discussed here correlate well with previous transmembrane conductance (electrophysiology) results for perforin pore formation[21,22].

Our findings on perforin pore assembly may explain its extraordinary efficiency in the context of the physiological immune synapse, where the disrupted target membrane is resealed through the exocytic repair response within seconds[23]. As a result, granzymes have a very short window of opportunity for diffusion into the target cell. By accelerating the pore assembly upon membrane insertion of small prepore assembly intermediates, as proposed here, perforin can enhance the membrane damage – and thus granzyme influx – before exocytic membrane repair is completed. One may even speculate that within a spatially restricted immune synapse, the growing pores may lead to localized plasma membrane rupture, which would further facilitate the diffusion of granzymes. Here it is worth noting that cytotoxic lymphocytes are serial killers capable of destroying several targets in quick succession; hence an efficient utilisation of intracellular perforin reservoirs is critical for immune surveillance. Indeed, the loss of perforin correlates with a failure to induce apoptosis in target cells, and prolongs the duration of the otherwise very brief immune synapse by a factor of 5 on average[33]. In humans, this leads to a hyperinflammatory and often fatal immune response. In physiological context, the results in Fig. 4 are particularly noteworthy, by showing how functionally impaired, dominant-negative TMH1-lock perforin affects the pore-forming functionality of WT perforin and the killing of target cells by cytotoxic T lymphocytes: In mice and humans, partial perforin deficiency has been associated with an increased predisposition to cancer[1].

## Conclusion

In summary, perforin initially forms loosely but irreversibly bound, short prepore oligomers on the target membrane. Upon insertion into the membrane, these short oligomers recruit additional prepore oligomers. Short membrane-inserted oligomers thus act as nucleation sites that promote further assembly growth into larger arc- and ring-shaped transmembrane pores with tighter subunit packing. This pathway is different from the prevalent assembly mechanism for bacterial toxins of the related CDC family, and provides a molecular basis for the speed and efficiency with which the immune system perforates virus-infected and cancerous cells. In addition, we find that pore formation by functional perforin is impeded by co-assembly with non-inserting mutant perforin, leading us to speculate that a similar effect underlies the pathologies related to partial perforin deficiency. Finally, we note that a similar growing-pore assembly pathway is likely and has been suggested for the MAC, given its initiation by anchoring C5b-C8 to the membrane, followed by the attachment of multiple copies of C9[16,17,19,20]. Our understanding of these assembly pathways will guide further structural studies of immune effectors, thus helping to identify targets for drugs that promote or suppress the immune response as required.

## Methods

### Protein expression and mutagenesis

Potential disulphide-lock mutations were initially identified using the programme Disulfide by Design (version 1.2)[34] based on the published structure of perforin[15]. A refined list of mutations was based on regions of conserved sequence across perforin sequences from vertebrate organisms and conserved structural features between perforin and C6. Recombinant mouse WT and TMH1-lock mutant (A144C-W373C) were expressed in baculovirus-infected Sf21 cells and purified from the supernatant as described by Voskoboinik et al.[35] All batches of WT and mutant perforin were produced simultaneously and had a similar yield (at least 200 ng/µL). No protein degradation was observed; when expressed in Rat Basophilic Leukemia cells[26], WT and TMH1-lock mutant had similar levels of expression, and there was no apparent difference in their storage in a secretory compartment, as assessed by endoglycosidase H resistance[36].

### Mass spectrometry

Mass spectrometric analysis was carried out to verify the presence of a disulphide-lock in the TMH1-lock mutant (Supplementary Fig. 1). For this purpose, histidine-tagged perforin (approximately 5 µg for both WT and TMH1-lock) was reduced with 50 mM DTT for 10 min at room temperature in 20 µL buffer (270 mM imidazole, 300 mM NaCl, 50 mM Tris pH 8). Equivalent samples of each protein were treated similarly without DTT (oxidised perforin). Perforin preparations were de-salted by precipitation with ice-cold methanol/chloroform[37], then resuspended in 2% formic acid for mass spectrometric analysis.

The protein was resolved on an Aeris high performance liquid chromatograph (HPLC) using a Widepore C4 phase (2.1 x 150 mm) with 3.6 µm particles (both Phenomenex, Torrance, CA, USA). The HPLC was coupled directly to an Agilent 6220 electrospray ionisation time-of-flight (ESI-TOF) mass spectrometer (Agilent Technologies, Palo Alto, CA, USA). HPLC was run in the presence of 0.1% formic acid, with bound protein eluted with a linear gradient from 0 – 90% acetonitrile at a flow rate of 0.25 mL/min. Acquisition was performed using the Agilent Mass Hunter Acquisition software version B.02.01 (B2116.30). Mass spectrometer settings were: Ionisation mode: electrospray ionisation, positive ion mode; drying gas flow: 7 L/min; nebuliser: 35 psi; drying gas temperature: 325°C; capillary voltage (Vcap): 4000 V; fragmentor: 250 V; skimmer: 65 V; OCT RFV: 250 V; scan range acquired: 100–3000 m/z; internal reference ions: Positive Ion Mode = m/z = 121.050873 & 922.009798.

The resultant m/z ion series was de-convoluted using Mass Hunter Analysis software (version B.03.01) to generate the observed masses for the ionisable species in the sample.

**Preparation of lipid vesicles**

Egg L-α-phosphatidylcholine (egg PC), cholesterol, 1,2-dioleoyl-*sn*-glycero-3-phosphocholine (DOPC) and sphingomyelin (SM) were purchased from Avanti Polar Lipids (Alabaster, AL, USA). Small unilamellar lipid vesicles were prepared by the extrusion method as described by Hope et al.[38] Briefly, lipids in powdered form were weighed and dissolved in a chloroform resistant container to produce a homogeneous mixture with a lipid concentration of ~1 mg/mL. The solvent was then slowly evaporated for 4 hours by passing a steady stream of nitrogen in a fume hood, yielding a dry lipid film. The lipid film was resuspended in 1 mL of 20 mM HEPES, 150 mM NaCl, pH 7.8, by vigorous vortexing for 5 minutes, to form large, multilamellar vesicles. This solution was transferred to a Fisherbrand FB11201 bath sonicator (Fisher Scientific, Loughborough, UK), maintained above the gel-liquid transition temperature of the constituent lipids. The large multilamellar vesicles were disrupted by 15-minute sonication treatments at frequencies between 37 – 80 kHz, interspersed by two freeze/thaw cycles. The solution containing the lipid dispersion was loaded into an Avanti mini-extruder kit (Avanti Polar Lipids) and kept above the gel-liquid transition temperature of the lipids at all times. The lipid solution was forced through a Whatman Nucleopore polycarbonate filter (GE Healthcare Lifesciences, Buckinghamshire, UK) with a 50 nm nominal pore diameter and the extrusion process repeated at least 30 times to yield small unilamellar vesicles.

**AFM sample preparation**

Between 1 – 4 µL of the small unilamellar vesicles (prepared as described above) were injected onto a freshly cleaved mica surface (Agar Scientific, Essex, UK) in the presence of 65 µL of an adsorption buffer consisting of 20 mM HEPES, 150 mM NaCl, 25 mM $MgCl_2$, 5 mM $CaCl_2$, pH 7.8. Thirty minutes incubation allowed the vesicles to rupture and adsorb onto the mica surface, yielding an extended lipid bilayer film (well above the gel-liquid transition temperature of the lipids). Excess vesicles in the supernatant were removed by rinsing with the adsorption buffer. The rinsing process was gently repeated 3–7 times to ensure a clean and uniform surface conducive for AFM imaging.

Perforin was injected directly onto supported lipid bilayers in the adsorption buffer, and incubated for 15 min at 37 °C unless stated otherwise, prior to imaging. For experiments with phase separated DOPC:SM:cholesterol 1:1:1 (molar ratio) lipids, the incubation and imaging temperature was maintained at 27 °C. The injected concentration of perforin ranged between 20 to 500 nM in 150 µL of the adsorption buffer.

For the doping assays (Fig. 4), wild-type and TMH1-lock perforin were mixed in the desired molar ratios in solution and injected, at a final concentration of 50-300 nM of the protein mixture, on the lipid bilayers at 37 °C and incubated for 15 min. Locked suilysin (Supplementary Fig. 5) was injected under the same conditions as perforin, at a concentration of 2 µM.

For unlocking the membrane-bound TMH1-lock perforin and suilysin (Supplementary Figs. 2, 5-6) prior to imaging, the mutant protein was incubated on the membrane with 2 mM DTT for 10 min at 37

°C. For observing the unlocking of membrane-bound TMH1-lock perforin while imaging and after it had been incubated on the membrane, 4 mM of DTT was added directly into the solution in the AFM fluid cell at 27 °C.

In the fixation experiments, labelled "+GA" where applicable, membrane-bound WT and TMH1-lock perforin were incubated 10 min with 0.04% glutaraldehyde (Sigma-Aldrich) at room temperature. Following fixation, the sample was washed with excess buffer before AFM imaging.

## AFM imaging and data processing

All images were recorded by force-distance curve based imaging (PeakForce Tapping) on a MultiMode 8 system (Bruker, Santa Barbara, CA, USA). The force-distance curves were recorded at frequencies between 2 - 4 kHz and a maximum tip-sample separation between 5 - 20 nm. The recorded topographic features were verified for consistency between trace and retrace. Images were typically recorded at 0.2 - 1 frame/min on an E scanner with temperature control.

Images analysis was performed either on the Nanoscope Analysis software version 1.70 (Bruker) or using the open-source SPM analysis software, Gwyddion version 2.37 (www.sourceforge.net). Raw AFM images were plane-levelled and line-by-line flattened using the lipid membrane as reference. A Gaussian filter with a full-width-half-maximum of 2-pixels (with a typical pixel size of 2 nm) was applied to smooth out high frequency noise where necessary. In all images, except for Fig. 1, the full z colour scale (see inset in Fig. 2b) was fixed at 25 nm with the limits set at -9 nm and 16 nm, relative to the top surface of the lipid bilayer (= 0 nm).

Height values indicated in the manuscript are given with ±10% confidence intervals, with the uncertainty mainly due to the flexible nature of the perforin assemblies. Static assemblies are more robust against the AFM imaging force, and in general appear slightly higher than more mobile features; similarly, densely packed assemblies may appear slightly higher than isolated assemblies.

We used commercial silicon nitride MSNL cantilevers (Bruker) with nominal spring constants ranging from 0.1 – 0.7 N/m and resonance frequencies between 10–35 kHz in liquid. Batches of AFM probes were screened for tip sharpness and appropriate tilt angles prior to data collection. Images recorded typically varied between 600 and 1200 nm in size at resolutions between 256-640 pixels per line.

The number of perforin pore subunits in images (Fig. 4) were determined by tracing their pore shapes with 3dmod 4.7.15 (Copyright 1994-2012 BL3DEMC & Regents of the University of Colorado)[43], and next converting the lengths to numbers of subunits using the experimentally determined subunit spacing. For the AFM data in (Fig. 4b), the errors were estimated based on the standard deviation (as a percentage of the average) for 28 AFM images from 4 different samples that had been incubated with WT perforin.

## Electron microscopy sample preparation, data acquisition and image processing

Negatively stained samples of perforin prepores and pores on lipid monolayers were prepared by largely following previously described procedures[39]. Solutions of monomeric mouse WT or TMH1-lock perforin were prepared at 2-5 μg/mL with the following buffer: 150 mM NaCl, 5 mM $CaCl_2$, 20 mM HEPES pH 7.8. The solutions were pipetted into Teflon wells as 30 μL droplets and coated with 1 μL of a 0.5 mg/mL lipid mixture containing 67 mol% egg PC and 33 mol% cholesterol in chloroform (both Avanti Polar Lipids). After solvent evaporation (~1 min) a non-glow-discharged gold electron microscopy grid (300 mesh, EMS, Hatfield, PA, USA), covered with a continuous carbon film, was placed on top of a droplet. The Teflon block was incubated in a sealed humid environment at 37°C for 15-50 min. The grid was gently lifted off with forceps, washed with few drops of the buffer and stained with 2% uranyl acetate. To observe the unlocking of membrane-bound TMH1-lock perforin, 5 mM of DTT was added to the solution through a side port of the Teflon well after 15 min of incubation and the sample was transferred and stained with 2% uranyl acetate after a further 10 min of incubation.

Low dose micrographs were recorded on a Direct Electron DE-20 camera (Direct Electron, San Diego, CA, USA) using a Tecnai F20 microscope (FEI Company, Hillsboro, OR, USA) operating at an accelerating voltage of 200 keV and a magnification of 40,404x (1.58 Å/pixel) at the specimen level (defocus range: 0.4–0.9 μm).

EMAN2[40] was used for selection of 1,000-3,000 segments of the arcs and rings images for each perforin prepore and pore preparation. These segment images were aligned using SPIDER[41], analysed by multivariate statistical analysis in Imagic[42] and classified according to the segment curvature, subunit spacing, and staining. The class averages were refined by multi-reference alignment[41] and classes with the least variance and clear features, containing 8-23 individual images, were selected.

The inter-subunit spacing was determined from the spacing of the first autocorrelation peak arising from the repeating subunits in class averages of the perforin assemblies. This gave consistent subunit repeats from 30-59 class averages of each assembly type, from which the standard deviations were determined. For early and late prepores, averages suitable for this analysis represented 34% and 39%. The remaining assemblies were harder to analyse because of the heterogeneity of the oligomers. Similar percentages of the data were analysed for pores: 32% for the WT and 35% for the unlocked perforin mutant pores.

Perforin arc and ring length distributions were determined by tracing their shapes with 3dmod 4.7.15 (Copyright 1994-2012 BL3DEMC & Regents of the University of Colorado)[43], and next converting the lengths to numbers of subunits using the experimentally determined subunit spacing.

## Cell based assays

Sheep red blood cell lysis assays were conducted at 37 $^{o}$C in 150mM NaCl, 1mM $CaCl_2$, 10mM HEPES pH 7.4 buffer; the release of haemoglobin was estimated by measuring absorbance at 405 nm wavelength as described in Voskoboinik et al.[26] For unlocking the TMH1-lock perforin in these cell based assays, protein (TMH1-lock, and WT for controls) was incubated with 4-50 mM DTT after TMH1-binding to the cells at 37°C (see Supplementary Fig. 2).

TMH1-lock mutant cDNA was cloned into the MSCV-IRES-eGFP vector and co-transfected with the packaging vector pCL-Eco (Addgene, Cambridge, MA, USA) into HEK293T cells. An empty MSCV-IRES-eGFP vector was used as control (no TMH1-lock expressed, only endogenous WT). Virus-containing supernatants were collected 48 hours later and immobilised on Retronectin (Takara Bio Inc., Kusatsu, Shiga Prefecture, Japan) coated cell culture plates for 4 hours. Primary cytotoxic T lymphocytes were isolated from the spleen of C57BL/6 mice that are transgenic for an ovalbumin T cell receptor (OT1) that recognises the peptide antigen SIINFEKL presented on syngeneic MHC class I (H-2K$^b$). The naïve cells were added to the Retronectin-virus coated plates and activated using 10 ng/mL SIINFEKL peptide and 100 units/mL IL-2 (Sigma Aldrich) for 3-4 days. Transduced eGFP$^+$ cells were isolated by fluorescence-activated cell sorting, and their cytotoxicity assessed (using syngeneic SIINFEKL-pulsed EL4 target cells) in a $^{51}$Cr release assay, as described in Voskoboinik et al.[44] All cell lines had been tested for mycoplasma contamination.

### Fluorescence recovery after photobleaching and estimates of membrane fluidity

DOPC:cholesterol 2:1 and DOPC:SM:cholesterol 1:1:1 (molar ratio) supported lipid bilayers were fluorescently labelled with 0.5 mol % Topfluor® PC lipid (all Avanti Polar Lipids), in 35 mm glass bottom cell culture dishes (MatTek Corporation, Ashland, MA, USA), in which the 10 mm glass window was replaced by mica to best reproduce the conditions of the AFM experiments. Lipid bilayer deposition on mica was achieved by vesicle fusion as described above. Lipid bilayers were imaged on a FV1200 confocal microscope equipped with a 100x/1.40 oil immersion objective (both Olympus Corporation, Tokyo, Japan), and a TC-324B automatic temperature controller (Warner Instrument Corporation, Hamden, CT, USA). The fluorescent bilayer was imaged with a 473 nm laser powered by a FV10-MCPSU (Olympus) at 1-2% output power across 42 µm with a resolution of 512 pixels and an acquisition speed of 1.6 s per image. In case of DOPC:SM:cholesterol, the lipids were locally (pre-) bleached prior to the FRAP experiment to prevent the immobile fraction of fluorophores (e.g., at phase boundaries) from affecting the measurements, and allowed to recover for 40 minutes. FRAP was performed on a circular area of 16.4 µm diameter at the centre of an image for 2 s at a laser output of 80%.

The FRAP curve was double normalized according to Phair[45]. The normalized curve was fitted with the Soumpasis model for diffusion limited recovery[46]. The fit was performed in Matlab (Mathworks, Cambridge, UK), using a least absolute residues approach and the Levenberg-Marquardt algorithm. The diffusion constant $D$ was calculated from the relation $D = \omega^2/4\tau_D$, where $\tau_D$ is the characteristic diffusion time as obtained from the fit, and $\omega$ is the diameter of the bleaching spot. The resulting values for $D$ are in the 1-10 µm$^2$/s range found for lipid diffusion in other fluid supported lipid bilayers[47]. For two-dimensional diffusion, the root mean square distance follows from $\sqrt{\langle r^2 \rangle} = \sqrt{4Dt}$, and was here calculated for $t = 60$ s, to give an estimate of the distance travelled at the time scale of a single AFM image.

We can apply Sackman's result for lateral diffusion in supported lipid bilayers[48] to extrapolate the measured diffusion of single lipids (with in-plane diameter $\phi$ of a few Å) to the diffusion of membrane patches that are of sufficient size to support entire perforin assemblies (with in-plane diameter $\phi$ of a few 10s of nm, ~100× the diameter of the individual lipids). Specifically, the scaling relations $D \propto \phi^{-2}$ and thus $\sqrt{\langle r^2 \rangle} \propto \phi^{-1}$ here provide lower bounds for the diffusion of such membrane patches.

**Data availability statement**

The authors declare that the data supporting the findings of this study are available within the paper and its supplementary information. Additional data and source files are available from the corresponding authors upon reasonable request.

## References

1. Voskoboinik, I., Whisstock, J. C. & Trapani, J. A. Perforin and granzymes: function, dysfunction and human pathology. *Nature Reviews Immunology* **15**, 388 (2015).
2. Reboul, C. F., Whisstock, J. C. & Dunstone, M. A. Giant MACPF/CDC pore forming toxins: A class of their own. *Biochimica et Biophysica Acta* **1858**, 475 (2015).
3. Lukoyanova, N., Hoogenboom, B. W. & Saibil, H. R. The membrane attack complex/perforin and cholesterol-dependent cytolysin (MACPF/CDC) superfamily of pore forming proteins. *Journal of Cell Science* **129**, 2125 (2016).
4. Shatursky, O. et al. The mechanism of membrane insertion for a cholesterol-dependent cytolysin: A novel paradigm for pore-forming toxins. *Cell* **99**, 293 (1999).
5. Shepard, L. A., Shatursky, O., Johnson, A. E. & Tweten, R. K. The mechanism of pore assembly for a cholesterol-dependent cytolysin: Formation of a large prepore complex precedes the insertion of the transmembrane beta-hairpins. *Biochemistry* **39**, 10284 (2000).
6. Hotze, E. M. et al. Arresting pore formation of a cholesterol-dependent cytolysin by disulfide trapping synchronizes the insertion of the transmembrane ss-sheet from a prepore intermediate. *Journal of Biological Chemistry* **276**, 8261 (2001).
7. Czajkowsky, D. M., Hotze, E. M., Shao, Z. F. & Tweten, R. K. Vertical collapse of a cytolysin prepore moves its transmembrane beta-hairpins to the membrane. *EMBO Journal* **23**, 3206 (2004).
8. Ramachandran, R., Tweten, R. K. & Johnson, A. E. The domains of a cholesterol-dependent cytolysin undergo a major FRET-detected rearrangement during pore formation. *Proceedings of the National Academy of Sciences of the United States of America* **102**, 7139 (2005).
9. Tilley, S. J., Orlova, E. V., Gilbert, R. J. C., Andrew, P. W. & Saibil, H. R. Structural basis of pore formation by the bacterial toxin pneumolysin. *Cell* **121**, 247 (2005).

10. Leung, C. et al. Stepwise visualization of membrane pore formation by suilysin, a bacterial cholesterol-dependent cytolysin. *eLife* **3**, e04247 (2014).
11. Sonnen, A. F. P., Plitzko, J. M. & Gilbert, R. J. C. Incomplete pneumolysin oligomers form membrane pores. *Open Biology* **4**, 140044 (2014).
12. Podobnik, M. et al. Plasticity of listeriolysin O pores and its regulation by pH and unique histidine. *Scientific Reports* **5**, 9623 (2015).
13. Mulvihill, E., van Pee, K., Mari, S. A., Muller, D. J. & Yildiz, O. Directly observing the lipid-dependent self-assembly and pore-forming mechanism of the cytolytic toxin listeriolysin O. *Nano Letters* **15**, 6965 (2015).
14. Ruan, Y., Rezelj, S., Zavec, A. B., Anderluh, G. & Scheuring, S. Listeriolysin O membrane damaging activity involves arc formation and lineaction - implication for *Listeria monocytegenes* escape from phagocytic vacuole. *PLOS Pathogens* **12**, e1005597 (2016).
15. Law, R. H. P. et al. The structural basis for membrane binding and pore formation by lymphocyte perforin. *Nature* **468**, 447 (2010).
16. Dudkina, N. V. et al. Structure of the poly-C9 component of the complement membrane attack complex. *Nature Communications* **7**, 10588 (2016).
17. Serna, M., Giles, J. L., Morgan, P. & Bubeck, D. Structural basis of complement membrane attack complex formation. *Nature Communications* **7**, 10587 (2016).
18. Lukoyanova, N. et al. Conformational changes during pore formation by the perforin-related protein pleurotolysin. *PLOS Biology* **13**, e1002049 (2015).
19. Scibek, J. J., Plumb, E. P. & Sodetz, J. M. Binding of Human Complement C8 to C9: Role of the N-Terminal Modules in the C8α Subunit. *Biochemistry* **41**, 14546 (2002).
20. Aleshin, A. E. et al. Structure of complement C6 suggests a mechanism for initiation and unidirectional, sequential assembly of membrane attack complex (MAC). *Journal of Biological Chemistry* **287**, 10210 (2012).
21. Metkar, S. S. et al. Perforin oligomers form arcs in cellular membranes: a locus for intracellular delivery of granzymes. *Cell Death and Differentiation* **22**, 74 (2015).
22. Praper, T. et al. Human perforin employs different avenues to damage membranes. *J Biol Chem* **286**, 2946 (2011).
23. Lopez, J. A. et al. Perforin forms transient pores on the target cell plasma membrane to facilitate rapid access of granzymes during killer cell attack. *Blood* **121**, 2659 (2013).
24. Hodel, A. W., Leung, C., Dudkina, N. V., Saibil, H. R. & Hoogenboom, B. W. Atomic force microscopy of membrane pore formation by cholesterol dependent cytolysins. *Current Opinion in Structural Biology* **39**, 8 (2016).
25. Gilbert, R. J. C., Mikelj, M., Dalla Serra, M., Froelich, C. J. & Anderluh, G. Effects of MACPF/CDC proteins on lipid membranes. *Cellular and Molecular Life Sciences* **70**, 2083 (2013).

26. Voskoboinik, I. et al. Calcium-dependent plasma membrane binding and cell lysis by perforin are mediated through its C2 domain. *Journal of Biological Chemistry* **280**, 8426 (2005).
27. Connell, S. D., Heath, G., Olmsted, P. D. & Kisil, A. Critical point fluctuations in supported lipid membranes. *Faraday Discussions* **161**, 91 (2013).
28. Antia, R., Schlegel, R. A. & Williamson, P. Binding of perforin to membranes is sensitive to lipid spacing and not headgroup. *Immunology Letters* **32**, 153 (1992).
29. Hotze, E. M. et al. Monomer-Monomer Interactions Propagate Structural Transitions Necessary for Pore Formation by the Cholesterol-dependent Cytolysins. *Journal of Biological Chemistry* **287**, 24534 (2012).
30. Traore, D. A. K. et al. Defining the interaction of perforin with calcium and the phospholipid membrane. *Biochemical Journal* **456**, 323 (2013).
31. Salvador-Gallego, R. et al. Bax assembly into rings and arcs in apoptotic mitochondria is linked to membrane pores. *EMBO Journal* **35**, 389 (2016).
32. Bavdek, A. et al. pH dependence of listeriolysin O aggregation and pore-forming ability. *FEBS Journal* **279**, 126 (2012).
33. Jenkins, M. R. et al. Failed CTL/NK cell killing and cytokine hypersecretion are directly linked through prolonged synapse time. *Journal of Experimental Medicine* **212**, 307 (2015).
34. Dombkowski, A. A. Disulfide by Design: a computational method for the rational design of disulfide bonds in proteins. *Bioinformatics* **19**, 1852 (2003).
35. Voskoboinik, I. et al. The functional basis for hemophagocytic lymphohistiocytosis in a patient with co-inherited missense mutations in the perforin (PFN1) gene. *Journal of Experimental Medicine* **200**, 811 (2004).
36. Brennan, A. J. et al. Protection from Endogenous Perforin: Glycans and the C Terminus Regulate Exocytic Trafficking in Cytotoxic Lymphocytes. *Immunity* **34**, 879 (2011).
37. Wessel, D. & Flügge, U. I. A method for the quantitative recovery of protein in dilute solution in the presence of detergents and lipids. *Analytical Biochemistry* **138**, 141 (1984).
38. Hope, M. J., Bally, M. B., Webb, G. & Cullis, P. R. Production of large unilamellar vesicles by a rapid extrusion procedure - characterization of size distribution, trapped volume and ability to maintain a membrane-potential. *Biochimica et Biophysica Acta* **812**, 55 (1985).
39. Dang, T. X., Hotze, E. M., Rouiller, I., Tweten, R. K. & Wilson-Kubalek, E. M. Prepore to pore transition of a cholesterol-dependent cytolysin visualized by electron microscopy. *Journal of Structural Biology* **150**, 100 (2005).
40. Tang, G. et al. EMAN2: An extensible image processing suite for electron microscopy. *Journal of Structural Biology* **157**, 38 (2007).
41. Frank, J. et al. SPIDER and WEB: Processing and visualization of images in 3D electron microscopy and related fields. *Journal of Structural Biology* **116**, 190 (1996).

42. van Heel, M., Harauz, G., Orlova, E. V., Schmidt, R. & Schatz, M. A new generation of the IMAGIC image processing system. *Journal of Structural Biology* **116**, 17 (1996).
43. Kremer, J. R., Mastronarde, D. N. & McIntosh, J. R. Computer visualization of three-dimensional image data using IMOD. *Journal of Structural Biology* **116**, 71 (1996).
44. Voskoboinik, I. et al. Perforin activity and immune homeostasis: the common A91V polymorphism in perforin results in both presynaptic and postsynaptic defects in function. *Blood* **110**, 1184 (2007).
45. Phair, R. D., Gorski, S. A. & Misteli, T. Measurement of dynamic protein binding to chromatin in vivo, using photobleaching microscopy. *Methods in Enzymology* **375**, 393 (2004).
46. Soumpasis, D. M. Theoretical analysis of fluorescence photobleaching recovery experiments. *Biophysical Journal* **41**, 95 (1983).
47. Ratto, T. V. & Longo, M. L. Obstructed diffusion in phase-separated supported lipid bilayers: A combined atomic force microscopy and fluorescence recovery after photobleaching approach. *Biophysical Journal* **83**, 3380 (2002).
48. Sackmann, E. Supported membranes: Scientific and practical applications. *Science* **271**, 43 (1996).

## Acknowledgements

This work has been funded by the BBSRC (BB/J005932/1, BB/J006254/1 and BB/N015487/1); the ERC (advanced grant 294408); the Wellcome Trust (079605/2/06/02); NHMRC Fellowship (1059126), Project (1062706) and Program (1013667) grants; and the Sackler Foundation. We thank Nitya Nand Gosvami and Joshua Pegman for assistance with early experiments and analysis, and Richard Thorogate, Annette Ciccone and Sandra Verschoor for technical support.

## Author contributions

C.L. designed, performed and analysed AFM experiments and co-wrote the paper. A.W.H. designed, performed and analysed AFM and FRAP experiments and co-wrote the paper. A.J.B. expressed mutant perforin, developed the TMH1-lock mutant, and carried out haemolysis experiments. N.L. carried out and analysed electron microscopy experiments and co-wrote the paper. S.T. performed and analysed haemolysis experiments. C.M.H. performed mass spectrometric analysis and co-wrote the paper. S.C.K., J.C.W. and M.A.D. contributed to the TMH1-lock mutant design. J.A.T. designed *in-vitro* experiments. I.V., H.R.S. and B.W.H. analysed the data, led the research and co-wrote the paper. All authors read and commented on the manuscript.

## Additional information

Supplementary information is available in the online version of the paper. Reprints and permission information is available online at www.nature.com/reprints. Correspondence and requests for materials should be addressed to I.V., H.R.S. and B.W.H.

## Figures

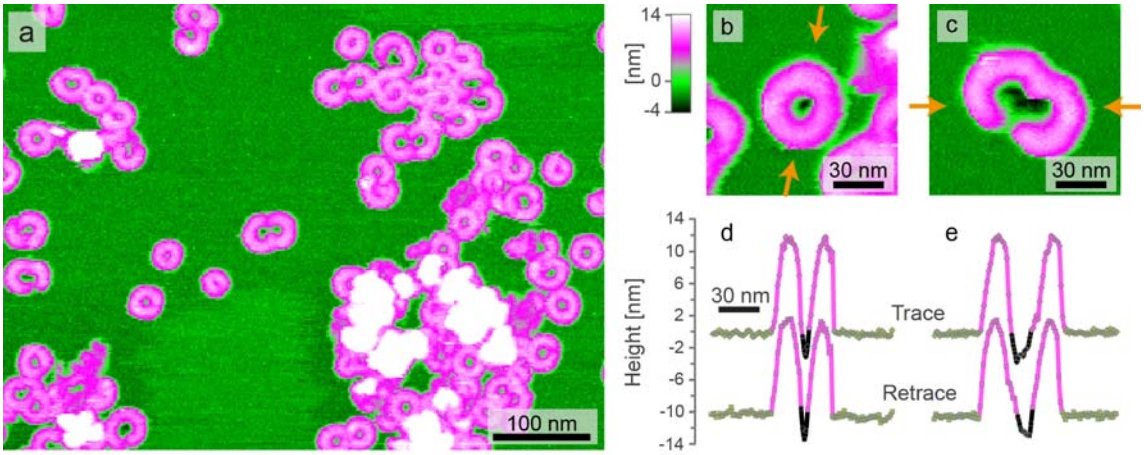

Figure 1. Membrane perforation by wild-type perforin, as imaged by AFM after completion of membrane pore formation. **a**, Perforin assemblies mostly appear as rings and clusters of arcs (purple/white), seen to preferentially bind to the lower (dark green), phosphatidylcholine-rich (PC-rich) domains of phase-separated DOPC:SM:cholesterol 1:1:1 supported lipid bilayers at T = 27 °C (see Methods). **b, c**, With larger magnification and sharp AFM probes, the AFM topography inside ring- and arc-shaped assemblies is measured below (black) the level of the membrane (green). **d, e**, This membrane perforation can be quantified by height profiles across assemblies, between the arrows in b and c, respectively. Line scans in both directions (trace/retrace, with retrace offset for clarity) are shown to validate the results.

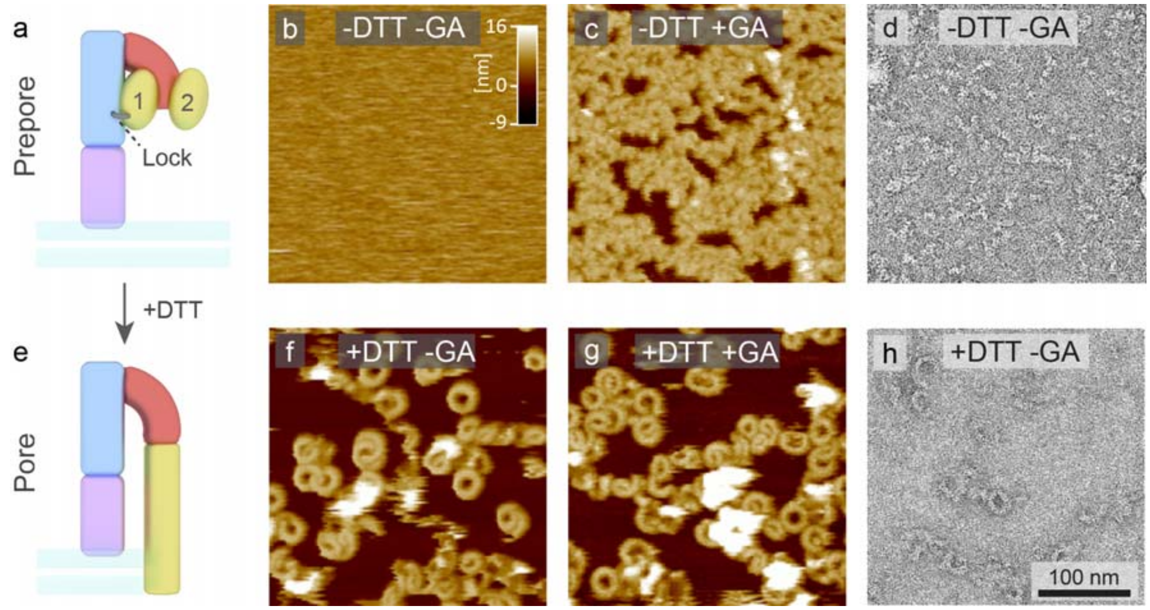

Figure 2. TMH1-lock mutant perforin forms prepores and pores on lipid membranes. **a**, Schematic showing the membrane-binding domain (purple), linked via the protein backbone (blue) and a central β-sheet (red) to the two TMH domains (yellow). The TMH domains ultimately unfurl to form the transmembrane β-barrel. **b, c**, AFM images of TMH1-lock perforin, without and with fixation by glutaraldehyde (GA, see Methods). **d**, Negative stain electron microscopy of the TMH1-lock perforin. **e**, The TMH1 domain is released upon subsequent exposure to DTT, allowing the mutant to form transmembrane pores. **f, g**, AFM images of unlocked mutant perforin, following exposure to DTT on the membrane, without and with fixation by glutaraldehyde. **h**, Negative stain electron microscopy of unlocked TMH1-lock perforin. AFM data were recorded on supported egg PC bilayers; electron microscopy data on monolayers that in addition to egg PC also contained 33% cholesterol. The protein was incubated on the membranes 15 min at 37 $^{o}$C prior to imaging at room temperature, and for f-h, prior to exposure to DTT. The scale bar in h applies to all AFM and electron microscopy images.

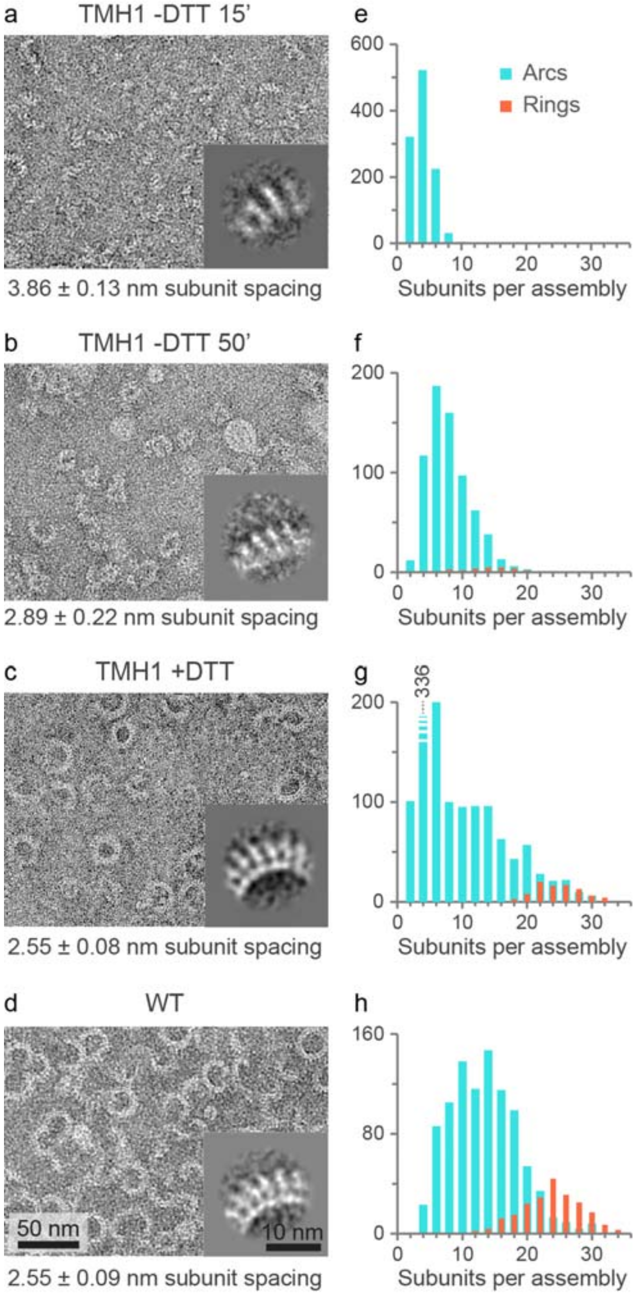

Figure 3. Evolution of perforin assembly on egg PC:cholesterol monolayers for TMH1-lock mutant perforin, compared to wild-type perforin pores. **a** and **b**, Negative stain electron microscopy images of TMH1-lock perforin prepores after 15 (a) and 50 min (b) incubation at 37 $^{o}$C. **c**, Pores formed by TMH1-lock perforin mutant after initial incubation for 15 min at 37 $^{o}$C followed by exposure to DTT. **d**, WT perforin, after 15 min incubation at 37 $^{o}$C. Insets in a-d show the corresponding averages of assembly segments. **e-h**, Corresponding oligomer length distributions as determined by tracing individual assemblies in electron microscopy images. Measured arc and ring lengths in nm were converted to numbers of subunits using the average subunit spacings shown in a-d.

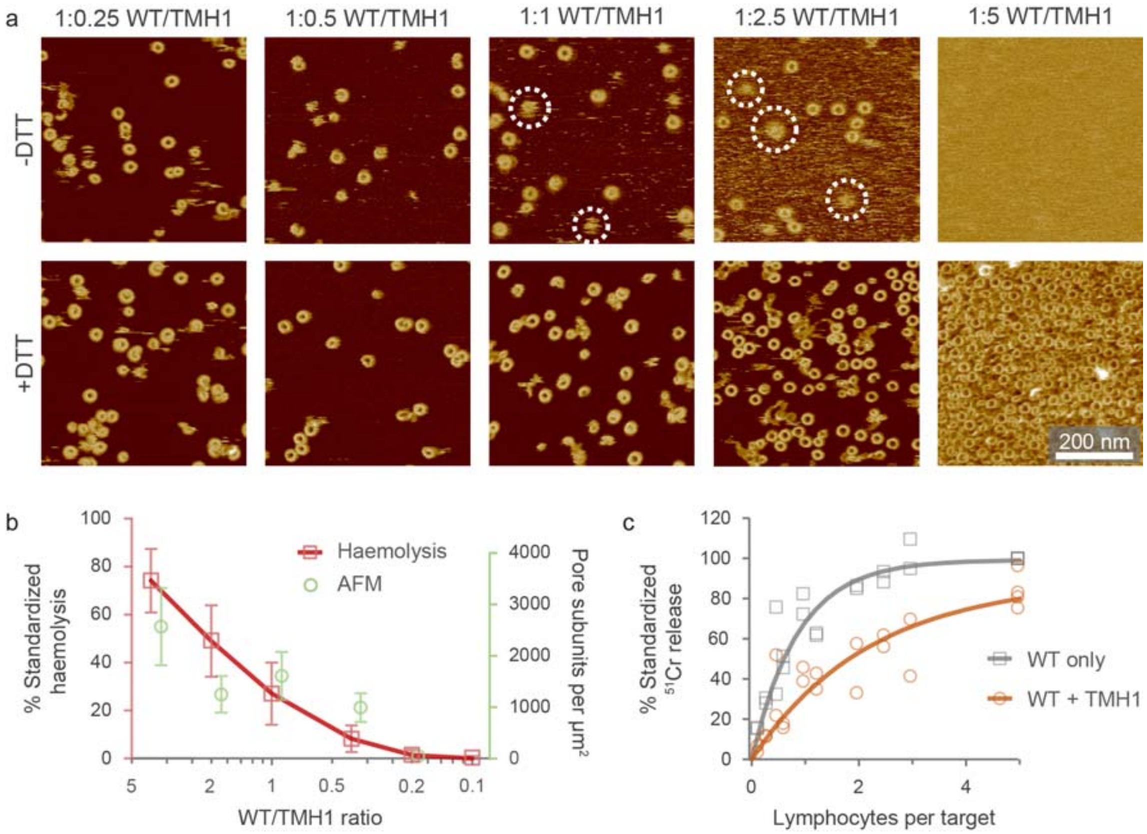

Figure 4. Effect of TMH1-lock mutant on pore formation by wild-type perforin. **a**, Columns show the AFM topography of the same samples before (-DTT) and after (+DTT) unlocking of the mutant on the egg PC membrane. Incubation and imaging conditions were as in Fig. 2b, f. Each column corresponds to a different ratio of WT and TMH1-locked perforin, with different amounts of TMH1-lock added to a fixed amount of WT perforin, as also illustrated by increasing amounts of pore assemblies from 1:0.25 to 1:5 in the bottom row (+DTT). Dotted circles mark examples of diffuse but discrete assemblies as discussed in the text. Colour scale: As in Fig. 2. **b**, Lysis of red blood cells for different ratios of WT and TMH1-lock perforin, where the amount of WT protein was kept constant. 100% corresponds to WT only. These data are consistent with the decrease in the amount of pore-state perforin as estimated based on AFM data as shown in a. Error bars indicate standard deviations. **c**, $^{51}$Cr cytotoxicity assays showing the reduced cytotoxicity for primary mouse activated cytotoxic T lymphocytes that co-express the TMH1-lock mutant in addition to endogenous WT perforin, compared to the empty-vector transduced cells. Shown are all the data points from 4 independent experiments. 100% refers to the $^{51}$Cr release at high 5:1 lymphocytes/target ratio, for the empty-vector transduced cytotoxic T lymphocytes in each independent experiment.

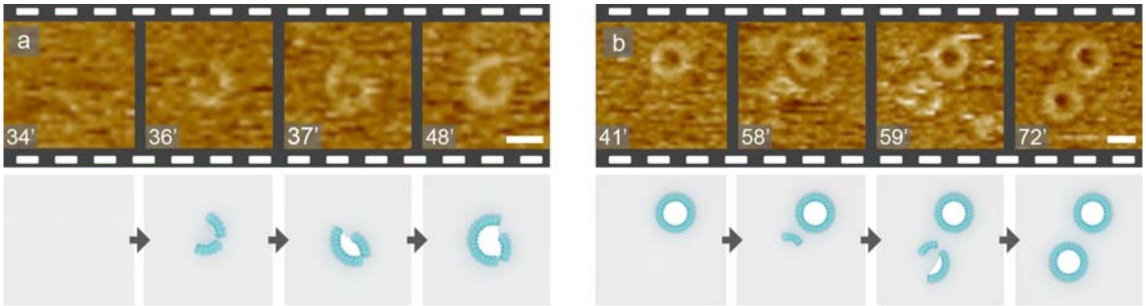

Figure 5. AFM of growing assemblies of wild-type perforin incubated and imaged at 27 $^{o}$C to slow pore formation compared with 37 $^{o}$C. **a**, Snapshots from a time sequence of a growing perforin assembly, with cartoons underneath to indicate the interpretation of growing pores. The diffuse, yellowish background is attributed to the diffuse, mobile prepores on the membrane, as in Fig. 2b and Supplementary Figs. 2b, 8a, 9a). For clarity, these mobile prepores are not shown in the cartoons. **b**, As a, snapshots from another assembly, starting to grow beside a ring-shaped assembly that is static and well resolved, indicating membrane perforation. In the cartoons, holes in the membrane are white, as compared to the grey membrane surface surrounding the assemblies. Scale bars: 20 nm. Colour scale: As in Fig. 2. Data were recorded on phase-separated DOPC:SM:cholesterol 1:1:1 supported lipid bilayers; see also Supplementary Figs. 8-10 and Supplementary Movies 2-6.

## Supplementary Movies

Supplementary Movie 1. The conversion of TMH1-lock perforin upon exposure to DTT on the membrane. Following preincubation of TMH1-lock protein on the membrane (see Methods), the mobile prepores convert to static pores upon exposure to DTT, as imaged here in real time by AFM.

Supplementary Movie 2. Sequence of AFM images showing how at a reduced temperature (27 $^{o}$C) perforin gradually converts from the mobile, diffuse prepore state to static pores. The image sequence is shown here 162 times accelerated compared to real time. Snapshots of this sequence are shown in Supplementary Fig. 9c-e.

Supplementary Movie 3. Sequence of AFM images showing the assembly of a perforin pore in real time at 27 $^{o}$C. The image sequence is shown here 162 times accelerated compared to real time. Snapshots of this sequence are shown in Fig. 5a.

Supplementary Movie 4. Sequence of AFM images showing the assembly of a perforin pore in real time at 27 $^{o}$C. The image sequence is shown here 162 times accelerated compared to real time. Snapshots of this sequence are shown in Fig. 5b.

Supplementary Movie 5. Sequence of AFM images showing the assembly of a perforin pore in real time at 27 $^{o}$C. The image sequence is shown here 162 times accelerated compared to real time. Snapshots of this sequence are shown in Supplementary Fig. 10a.

Supplementary Movie 6. Sequence of AFM images showing the assembly of a perforin pore in real time at 27 $^{o}$C. The image sequence is shown here 162 times accelerated compared to real time. Snapshots of this sequence are shown in Supplementary Fig. 10b.

# Real-time visualization of perforin nanopore assembly

Carl Leung[‡], Adrian W. Hodel[‡], Amelia J. Brennan[‡], Natalya Lukoyanova[‡], Sharon Tran, Colin M. House, Stephanie C. Kondos, James C. Whisstock, Michelle A. Dunstone, Joseph A. Trapani, Ilia Voskoboinik*, Helen R. Saibil* & Bart W. Hoogenboom*

[‡]These authors contributed equally to this work.

*Corresponding authors: ilia.voskoboinik@petermac.org (I.V.); h.saibil@mail.cryst.bbk.ac.uk (H.R.S.); b.hoogenboom@ucl.ac.uk (B.W.H.).

# Supplementary Information

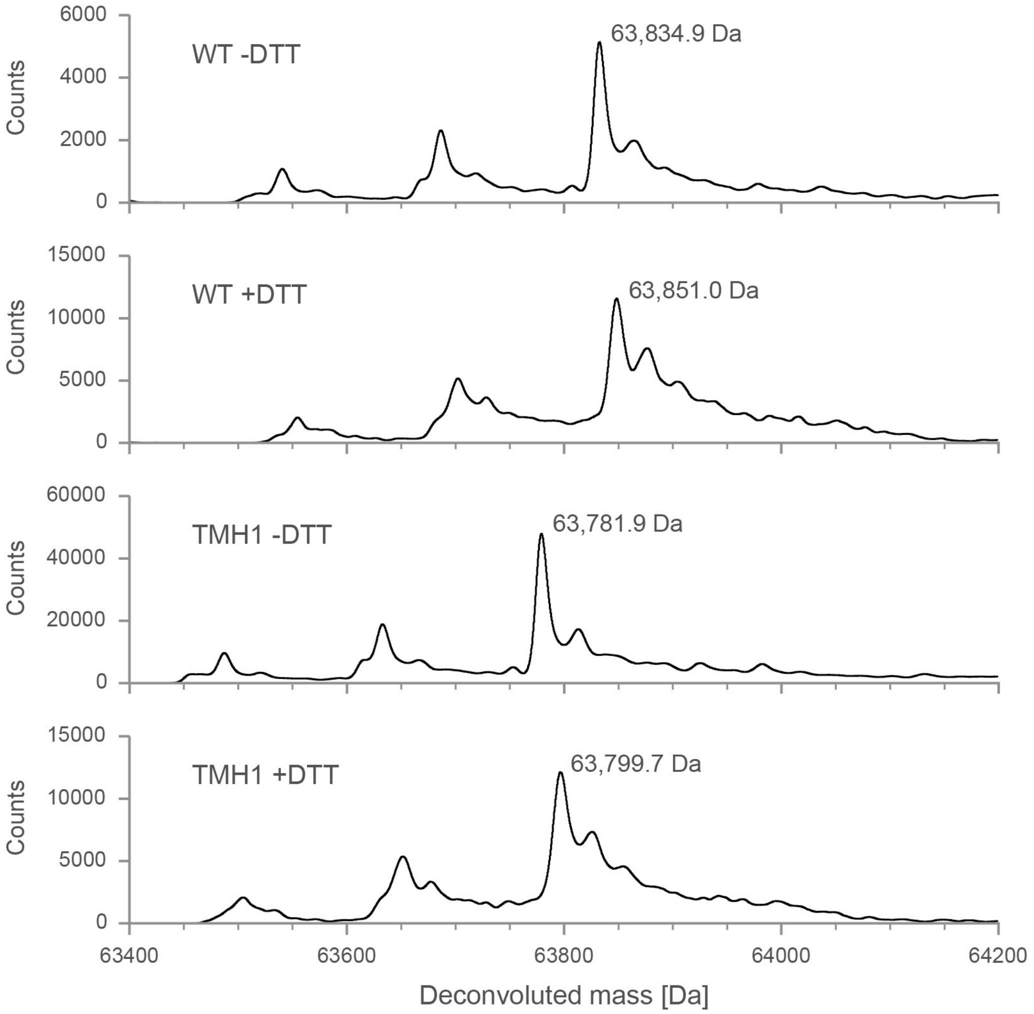

| | -DTT [Da] | +DTT [Da] | Difference [Da] | # S-S bonds |
|---|---|---|---|---|
| WT | 63,834.9 | 63,851.0 | 16.1 | 8 |
| TMH1-lock | 63,781.9 | 63,799.7 | 17.8 | 9 |
| Difference | 53.0 | 51.3 | | |

Supplementary Figure 1. ESI-TOF mass spectrometry of wild-type and TMH1-lock mutant (A144C-W373C) perforin, in their oxidized (-DTT) and reduced (+DTT) states. The mass assignments and mass differences are summarized in the table below. Attributing the difference between reduced and oxidized state to cysteine-bound protons only (2 per disulphide bond), we find that the A144C-W373C substitution has increased the number of disulphide bonds by one, as expected. In addition, the measured mass differences between WT and TMH1-lock protein also agree with the predictions (51 Da in the reduced state; 53 Da in the oxidized state), indicating that no additional moieties have bound to the protein because of the A144C-W373C substitution. At masses below the main peaks used for the mass assignments, two subsidiary maxima are observed, which can be attributed to proteins having lost one and two fucose residues (~147 Da) from the glycans. The estimated uncertainty for the mass attributions is ± 0.3 Da, and for the mass differences ± 0.4 Da.

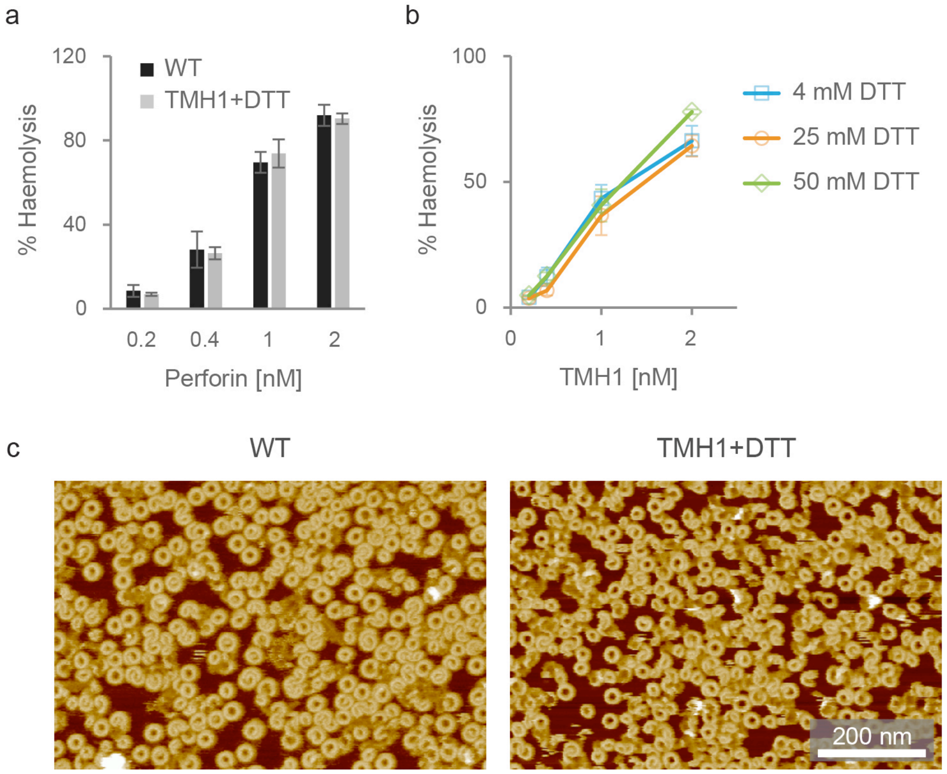

Supplementary Figure 2. Measurement of perforin activity for wild-type and for TMH1-lock mutant perforin that was exposed to DTT after binding to the membrane. **a**, Haemolysis for WT (-DTT) and TMH1-lock perforin (+4 mM DTT), with different amounts of added protein. **b**, Haemolysis assay demonstrating that the TMH1-lock perforin activity is insensitive to the DTT concentration between 4-50 mM under these conditions. **c**, AFM images of egg PC membranes that were incubated with identical concentrations (~200 nM) of WT perforin (-DTT) and TMH1-lock mutant perforin (+DTT), showing highly similar membrane coverage by perforin pores. Note that the perforin amount/concentration in the AFM experiments is typically higher than that in the haemolysis assays, to facilitate pore formation over the whole 80 $mm^2$ model membrane, whereas presumably only a part of the red blood cell membrane needs to be perforated to result in cell lysis. Error bars in a, b indicate the standard error of the mean, with $n = 6$ in a; and with $n = 4$ for 4 mM and 25 mM DTT, and $n = 3$ for 50 mM DTT in b.

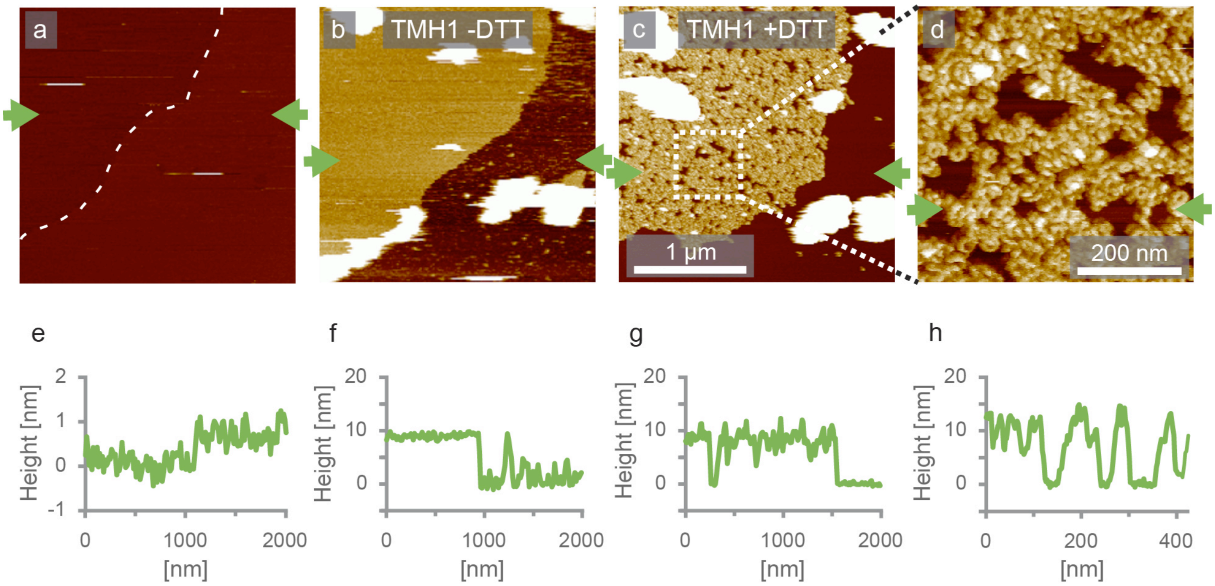

Supplementary Figure 3. TMH1-lock mutant perforin on phase-separated DOPC:SM:cholesterol 1:1:1 supported lipid bilayers. **a**, At T = 27 °C (see Methods), these membranes form different domains, with the DOPC-rich domains appearing 0.8 nm below the more densely packed SM-rich domains[25]. The dashed line indicates the phase boundary. **b**, The locked mutant (TMH1 -DTT) preferentially binds to the lower phase, forming plateaus that protrude 10 nm above the surrounding SM-rich domain, and thus 11 nm above the underlying membrane surface. **c, d**, On exposure of the same area to DTT, the TMH1 prepores transit to the pore state and can be resolved as static arcs and rings (here recorded 80 min after the injection of DTT). Due to their more static nature, they appear slightly higher than the prepores, 12 nm above the underlying membrane, in agreement with the pore structure as determined by cryo electron microscopy[11]. **e-h**, Height profiles along the lines marked by green arrows in the respective AFM images in a-d.

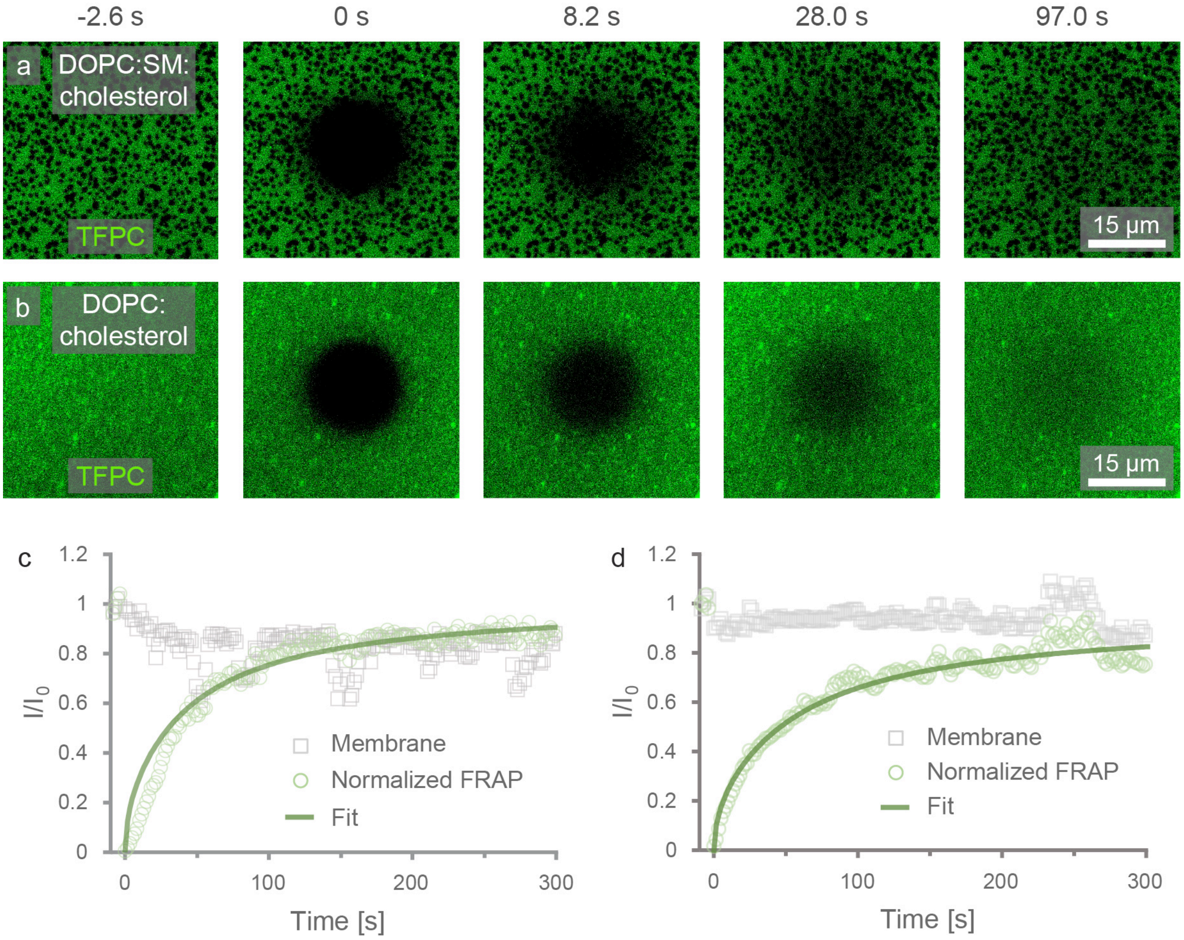

e

| Lipid composition | T [°C] | $\tau_{D,TFPC}$ [s] | $D_{TFPC}$ [μm²/s] | $\sqrt{\langle r^2_{60s} \rangle}$ [μm] |
|---|---|---|---|---|
| DOPC:SM:cholesterol | 27 | 35 ± 4.4* | 2.0 ± 0.3 | 22 ± 1.4 |
| DOPC:cholesterol | 27 | 45 ± 5.3* | 1.5 ± 0.2 | 19 ± 1.1 |

* 95% confidence bounds

Supplementary Figure 4. Fluorescence recovery after photobleaching to assess the fluidity of the lipid membrane. **a, b**, Fluorescently labelled PC (TFPC, see Methods) is shown to rapidly diffuse into bleached areas, both for phase-separated DOPC:SM:cholesterol 1:1:1 bilayers and for homogeneous DOPC: cholesterol 2:1 bilayers. The DOPC:SM:cholesterol bilayers were prepared identically as in the AFM experiments. Small dark spots scattered over the image correspond to the SM-rich domains; perforin predominantly binds to the PC-rich domains (see Fig. 1a), here bright. **c, d**, Fluorescence recovery curves for the DOPC:SM: cholesterol and DOPC: cholesterol membranes, respectively. **e**, Results of the fits in c, d, where the last column indicates the mean displacement of single lipids in 60 s, i.e., at the minute time scale of the AFM images. The predicted mean displacement of perforin assemblies is at least 1/100th of that of single lipids (see Methods), i.e., > 200 nm on a minute timescale, unless their mobility is constraint by perforin contact to the underlying mica substrate. Hence in the AFM images on PC-rich domains, static perforin assemblies must be transmembrane pores.

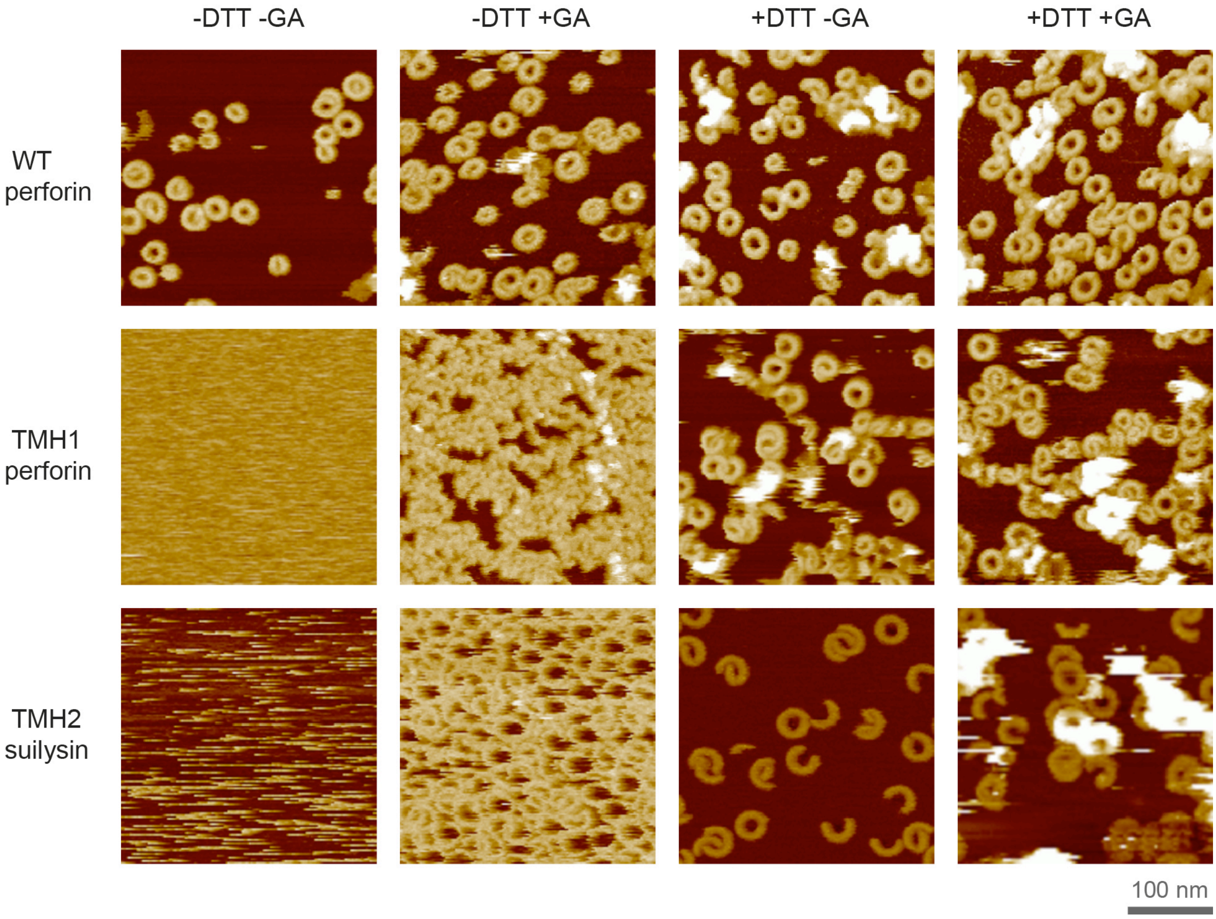

Supplementary Figure 5. Prepore and pore appearance depending on exposure to DTT and fixation with glutaraldehyde (GA), characterized by AFM. Top row: WT perforin is not visibly affected by DTT or glutaraldehyde. Middle row: TMH1-lock mutant perforin, here repeated from Fig. 2 to facilitate a direct comparison. Bottom row: The disulphide-locked TMH2-lock mutant of the CDC suilysin[10], for comparison. Without fixation, suilysin prepores appear less dense on the membrane than perforin prepores (-DTT -GA), but on fixation (-DTT +GA) are shown to consist of assemblies that are similar in size to the suilysin pores (+DTT +/-GA); this is consistent with the fact that CDC assembly is terminated in the prepore state. Here we find perforin to be different, with only smaller assemblies in the prepore state, and the assembly proceeding after triggering the prepore-to-pore transition. In general, we found that the glutaraldehyde treatment promotes the clustering of prepore assemblies, leading to the formation of micron-sized plaques on the membrane that are sufficiently immobile and dense to facilitate the prepore imaging in our AFM experiments. Hence also the higher protein densities in the images of TMH1 perforin and TMH2 suilysin prepores (-DTT +GA) compared to the pore state (+DTT +/-GA). Perforin data were recorded on egg PC membranes, suilysin data on egg PC:cholesterol 2:1 membranes.

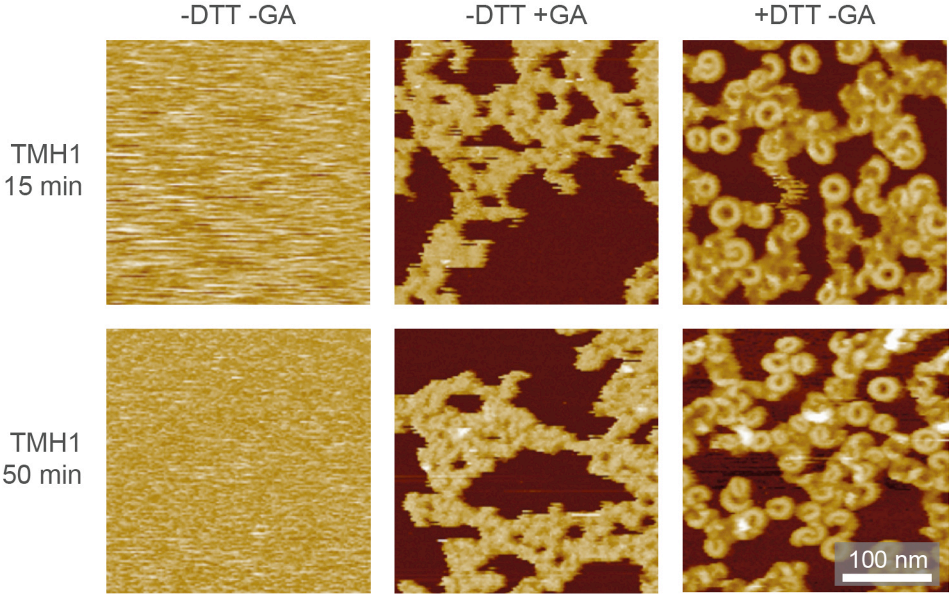

Supplementary Figure 6. AFM images for 15 and 50 min incubations (at 37 $^{o}$C) of egg PC membranes with TMH1-lock mutant perforin. Without glutaraldehyde fixation (-GA), the prepore state (-DTT) does not show any defined features, indicating high perforin mobility on the membrane, also after prolonged incubation. Fixed prepores (-DTT +GA) appear as short assemblies, different from the pore state (+DTT –GA) that is observed after addition of DTT, see also Fig. 2 and Supplementary Fig. 5.

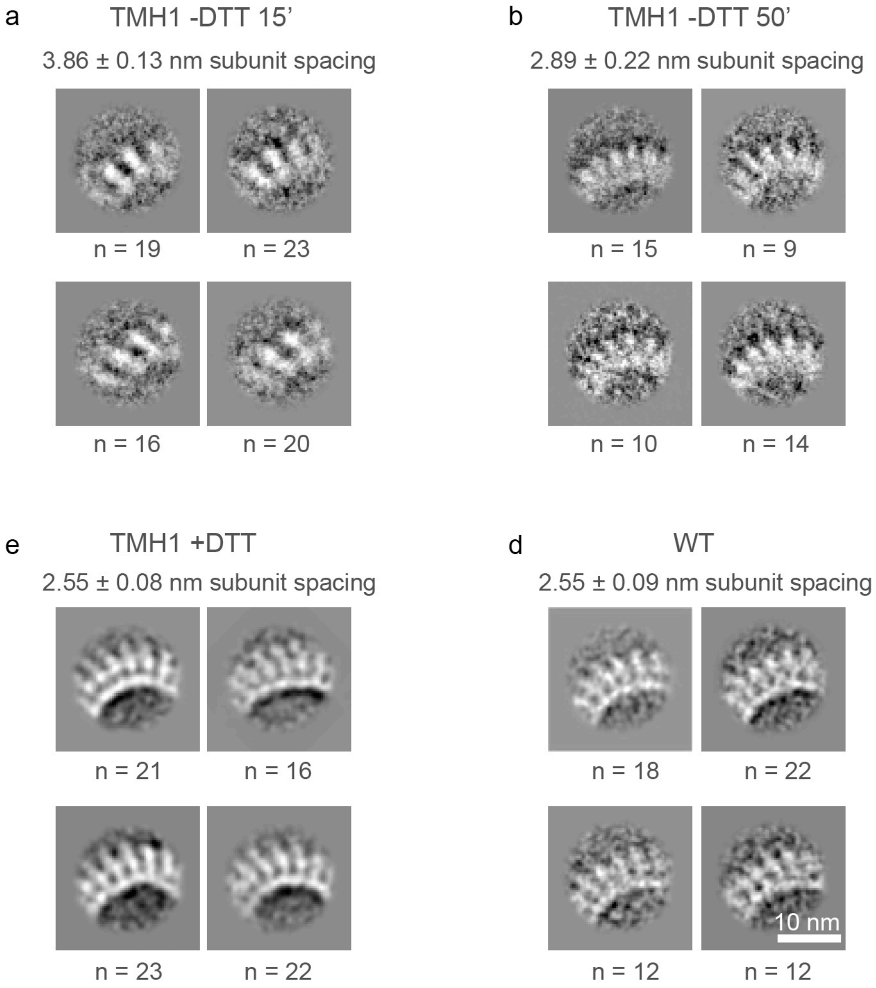

Supplementary Figure 7. Additional averages supporting the electron microscopy images in Fig. 3a-d. Four class averages are shown for each type of assembly, with the number of particles in each shown below. The averages and standard deviations of the inter-subunit spacing are given above each panel.

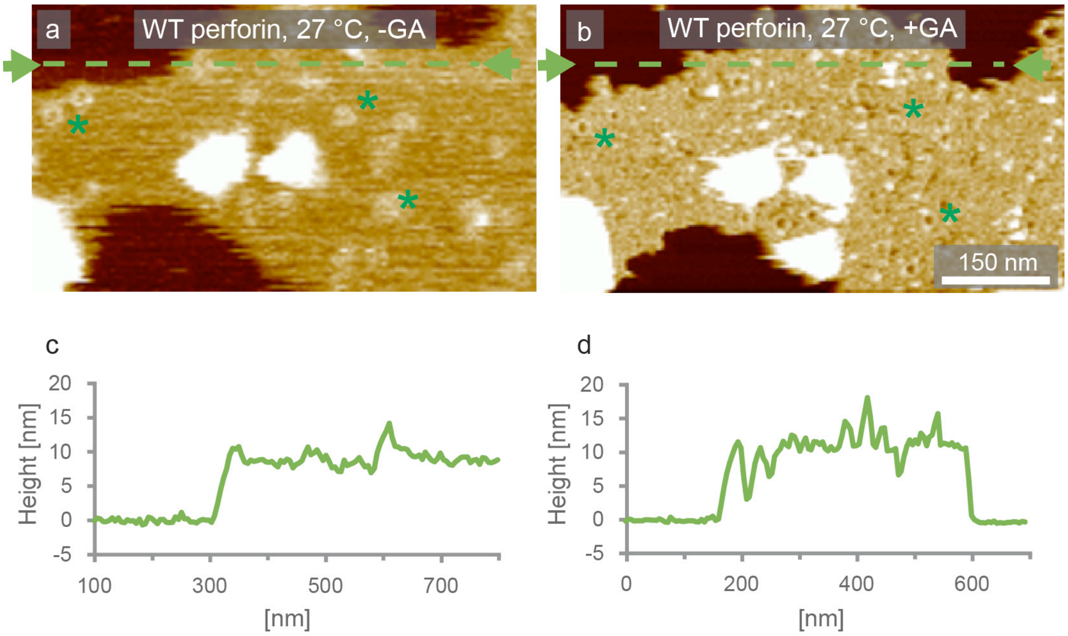

Supplementary Figure 8. AFM of wild-type perforin plateaus at early stages of membrane pore formation. **a**, Imaged 20 minutes after exposing a DOPC:SM:cholesterol 1:1:1 supported lipid bilayer to WT perforin at 27 °C, some pores can be clearly resolved in the diffuse protein background, whereas others are presumably only partially inserted into the membrane and appear as diffuse but static blobs, similar to the observations in Fig. 4a. **b**, Glutaraldehyde (GA) fixation stabilizes these assemblies for AFM imaging, and allows the blobs to be resolved as larger, mostly ring-shaped assemblies and the remaining diffuse background as shorter, presumably prepore assemblies. Green asterisks (*) mark examples of assemblies that are identified at the same locations before and after fixation. **c, d**, Height profiles along the lines indicated in a and b, respectively.

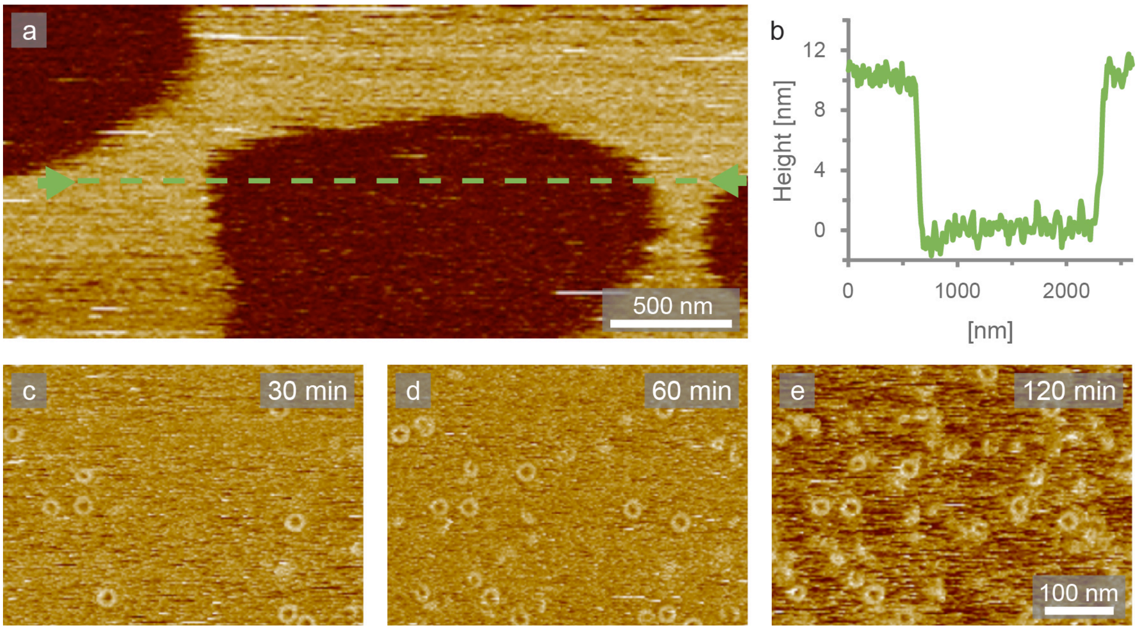

Supplementary Figure 9. Wild-type perforin incubated and imaged at 27 °C on phase-separated DOPC:SM:cholesterol 1:1:1 supported lipid bilayers. See Supplementary Fig. 3 for comparison with the TMH1-lock mutant under similar conditions. **a, b**, WT perforin initially forms diffuse plateaus on PC-rich domains, protruding 10 nm above the surrounding SM-rich domains, and thus 11 nm above the underlying membrane. **c-e**, imaged at higher magnification, the diffuse plateaus are gradually replaced by well-defined pores.

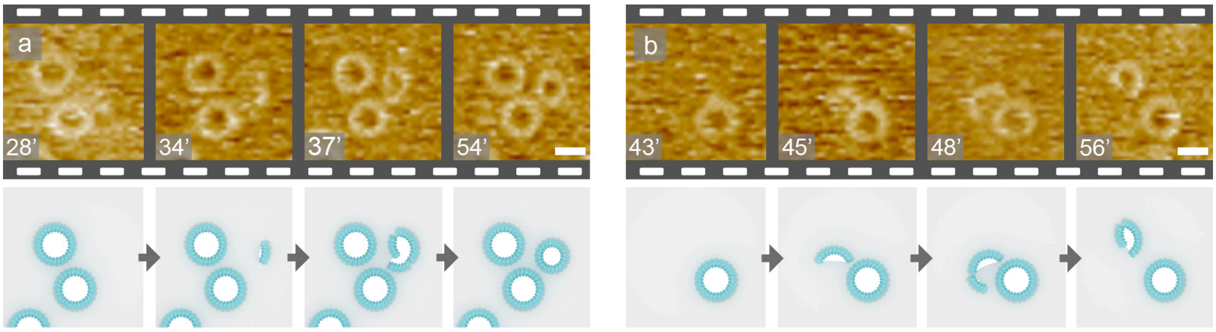

Supplementary Figure 10. AFM of growing assemblies of wild-type perforin incubated and imaged at 27 $^{o}$C to slow pore formation compared with 37 $^{o}$C, additional examples, represented as in Fig. 5. **a**, Snapshots from a time sequence of a growing perforin assembly, with cartoons underneath to indicate the interpretation of growing pores. The diffuse, yellowish background is attributed to the diffuse, mobile prepores on the membrane, as in Fig. 2b and Supplementary Figs. 2b, 8a, 9a). For clarity, these mobile prepores are not shown in the cartoons. **b**, as a, snapshots from another assembly, starting to grow beside a ring-shaped assembly that is static and well resolved, indicating membrane perforation. In the cartoons, holes in the membrane are white, as compared to the grey membrane surface surrounding the assemblies. Scale bars: 20 nm. Data were recorded on phase-separated DOPC:SM:cholesterol 1:1:1 supported lipid bilayers